

Multiple axon tracking for biohybrid brain computer interfaces from directional living neural networks

Thesis Subtitle

Author Name

A thesis presented for the degree of
Doctor of Philosophy

Department Name

University Name

Country

Date

1 Abstract

Lorem ipsum dolor sit amet, consectetur adipisicing elit, sed do eiusmod tempor incididunt ut labore et dolore magna aliqua. Ut enim ad minim veniam, quis nostrud exercitation ullamco laboris nisi ut aliquip ex ea commodo consequat. Duis aute irure dolor in reprehenderit in voluptate velit esse cillum dolore eu fugiat nulla pariatur. Excepteur sint occaecat cupidatat non proident, sunt in culpa qui officia deserunt mollit anim id est laborum. Lorem ipsum dolor sit amet, consectetur adipisicing elit, sed do eiusmod tempor incididunt ut labore et dolore magna aliqua. Ut enim ad minim veniam, quis nostrud exercitation ullamco laboris nisi ut aliquip ex ea commodo consequat. Duis aute irure dolor in reprehenderit in voluptate velit esse cillum dolore eu fugiat nulla pariatur. Excepteur sint occaecat cupidatat non proident, sunt in culpa qui officia deserunt mollit anim id est laborum. Lorem ipsum dolor sit amet, consectetur adipisicing elit, sed do eiusmod tempor incididunt ut labore et dolore magna aliqua. Ut enim ad minim veniam, quis nostrud exercitation ullamco laboris nisi ut aliquip ex ea commodo consequat. Duis aute irure dolor in reprehenderit in voluptate velit esse cillum dolore eu fugiat nulla pariatur. Excepteur sint occaecat cupidatat non proident, sunt in culpa qui officia deserunt mollit anim id est laborum.

Contents

1 Abstract	1
2 Introduction	5
2.1 Outline	6
2.2 Biohybrid neural interfaces	6
2.3 Engineered directional neural networks	8
2.4 Multiple object tracking	9
3 Methods and Materials	10
3.1 Experimental procedures	10
3.1.1 Dish preparation	10
3.1.2 Poly-D-Lysine & laminin coating	10
3.1.3 PDMS micro structure design, fabrication & mounting	11
3.1.4 Spheroid creation	12
3.1.5 Primary Cell Culture (EYLUL)	12
3.1.6 Retina Dissections (EYLUL)	12
3.1.7 AggreWell™ Preparation and Cell Dissociation (EYLUL)	12
3.1.8 Cell Seeding and Primary Neuronal Cell Culture (EYLUL)	13
3.1.9 Timelapse recording	13
3.2 Data analysis	13
3.2.1 Timelapse datasets	13
3.2.2 Initial timelapse processing	13
3.2.3 Axon growth cone labelling	14
3.2.4 Timelapse data preprocessing	15
3.2.5 Growth cone detection model	15
3.2.5.1 Temporal context frames	15
3.2.5.2 Tiling	17
3.2.5.3 Detection output format	17
3.2.5.4 Training procedure	17
3.2.5.5 Data association	18
3.2.6 Directionality inference from tracking	18
3.2.7 Directionality evaluation metric	19
3.2.8 Statistics	20
3.2.9 Between dataset variance	20
4 Results	20
4.1 Tracking performance	20
4.2 Micro structure designs	20
5 Discussion	23
5.1 Model architecture and generalization	23
6 Supplementary Information	24

List of Figures

1	Growth cone detection model overview	16
2	Growth cone tracking model performance	21
3	PDMS micro structure designs	22

List of Supplementary Figures

1	Initial timelapse preprocessing steps	25
2	Axon growth cone labelling	26
3	Labelled training data examples	27
4	Axon reconstruction from growth cone track	28

List of Tables

1	RGC medium composition	11
2	Overview of timelapse recording data	14
3	Minimum cost flow hyperparameters	19

List of Abbreviations

CLSM - Confocal laser scanning microscope PDMS CNN MOTA
DI deionized PDL PBS phosphate buffered saline CAD
CNS DBS
MEA
dLGN
MOT
R-CNN

2 Introduction

Think of this as the funnel into your results story. What does the reader need to know to understand the results. It should not feel like they come out of the blue. What's the context.

This can include: Which problem are you addressing?

For which domains is the addressed problem relevant?

The intro should roughly map to the results order: model -> 20 structure screen -> primitives

It. can. be. short.:)

I hate this pseudo sophisticated research jargon. I can't have that in my thesis. Please avoid it.

Broad scope approach-motivation statement

Funnel into short abstract-like summary of the project

background in three sections: biohybrid BCI, directional networks, MOT

research problem, research aims + presented solution, significance + which value

Why do we need directional neural networks? general entry funnel biohybrid interfaces disease models (sprinkle of bottom up neuroscience)

which efforts have been made to make networks directional? orient to csabas paper

Which solution does this work provide? primitives screen 20 test structures screen

2.1 Outline

Understanding the human brain requires neuroscience to develop complexity reducing model systems that capture relevant functional, anatomical or chemical features. The evaluation of which abstraction level and thus model system is appropriate for answering key functional questions about the brain has long been a source of controversy. This discussion is fundamentally rooted in the tension between losing essential features in overly simplified model systems, and dealing with overwhelming complexity and low experimental throughput in model systems more closely resembling the human brain.

Although this work broadly employs *in vitro* model systems thus trading off resemblance to real brains for higher throughput and reduced complexity, it is not primarily motivated by a certainty that this high abstraction level will indeed *solve* fundamental neuroscientific questions. Instead, this project aims to follow an approach that has led to notable progress in other domains, most prominently artificial intelligence: Developing an understanding of the system by engineering it. This method has found adoption in domains as neuromorphic engineering (Mead 1989) and neural engineering (Durand 2006), with the latter focusing i.a. on building technology from living neural systems. Guided by the engineering problems, the hope of these domains is that relevant neuroscientific questions are answered along the way. And even if this does not come true, advancement in these fields may still result in useful new technologies. The science presented here follows this pursuit.

You can only do engineering at that scale. that's why were at that scale. DId you make that clear enough? Inconsistency: you mention this here in the beginning but this idea is not really found throughout the introduction. Motivation is put on bad stimulation ability, and bad *in vitro* network models.

In this work, ... [abstract like but shorter] f

f
f
f
f
f
f
f

2.2 Biohybrid neural interfaces

Neuroelectric interfacing based on metal electrodes has made remarkable progress over the last decades (Maynard, Nordhausen, and Normann 1997, Jun et al. 2017). These technologies excel at locally confined high resolution neural recording for a time period on the order of weeks. However, given the immense challenges related to high quality neural interfacing (Stevenson and Kording 2011), naturally, existing recording and particularly stimulation technology exhibit shortcomings. The clinically most adapted CNS stimulation method, deep brain stimulation (DBS), does not specifically depolarize single neurons but instead exerts various modulatory effects on entire brain areas (Herrington, Cheng, and Eskandar 2016). Low spatiotemporal resolution may be tolerable for common DBS applications, however, addressing the clinically highly relevant cases of vision-, touch-, or hearing loss is currently limited by insufficient resolution (Tong et al. 2020). Another issue affecting both stimulation and conventional neural recording systems is the

induced foreign body response. Due to natural brain movement, rigid metal electrodes cause inflammation, neuronal cell death and glia formation while simultaneously, conventional electrode insulation undergoes biodegradation resulting in decreased impedance (Tresco and Winslow 2011, Saxena et al. 2013, Grill, Norman, and Bellamkonda 2009, Polikov, Tresco, and Reichert 2005). In research applications, central nervous system (CNS) stimulation is most commonly performed through optogenetic tools (Zemelman et al. 2002, Boyden et al. 2005). While the cell-type specificity of optogenetics can be of great value, the limitations in spatial resolution inherent to *in vivo* light-based technology seem to be a major hurdle for increasing spatial resolution. On top of this, the risk of genetic off-target effects and adeno associated virus (AAV) immune responses restrict medical use cases in the near term (Mendoza, El-Shamayleh, and Horwitz 2017).

Biohybrid implants take a fundamentally different approach to neural interfacing, drawing inspiration from tissue engineering and *in vitro* neuroscience. First described by Stieglitz et al. 2002, this promising technology aims to solve the latent issue of biocompatibility by moving towards the integration of biological components (Rochford et al. 2020). At the same time, biohybrid technology may benefit from the highly impressive *spec sheet* of a neuron, including energy efficiency, self-containment, and signal transmission properties. Whilst engineering with neural tissue presents almost daunting challenges, the biocompatibility prospects of biohybrid interfaces are currently unaccessible by competing technologies. CNS applications of the biohybrid approach include the coating of metal electrodes with host cells (Purcell et al. 2009, Faveri et al. 2014), and the use of ectopic axons as electrodes (Tang-Schomer et al. 2014, Adewole et al. 2021). The currently most advanced biohybrid implant is based on a hydrogel microcolumn containing ectopic cortical axons that are optogenetically driven through an light emitting diode (LED) optical fiber outside the brain (Adewole et al. 2021). While synapse formation was shown anatomically *in vitro*, the *in vivo* proof-of-concept implantation did not go as far as showing functional target tissue innervation.

Current biohybrid implants trade off biocompatibility for interface bandwidth and control. For example, the biohybrid implant presented in Adewole et al. 2021 relied on optically exciting the entire ectopically grown neural population, resulting in limited control of delivered stimulation. While this spatial resolution may be sufficient for specific use cases, this implant design offers insufficient control for delivering high dimensional data, such as sensory input. For addressing the pressing issue of functionally restoring sensory modalities (Bourne et al. 2021), a biohybrid implant needs to allow for stimulating independent channels. To solve this crucial design requirement, the implant presented here is based on a PDMS micro fluidic system enabling the independent stimulation of axons grown in micro channels. Briefly, PDMS membranes are placed on coated glass dishes and seeded with RGC spheroids. Axons extend through the 6 μm high channel system until they reach the 3 mm long output channel which will eventually be implanted. The final device will utilise stretchable AuTiO₂ nanowire electrical contact pads for stimulating RGC axons (Tybrandt et al. 2018). Long term host cell survival will be ensured by having the implant face the brain surface such that RGC spheroids are integrated with the CNS microenvironment. The device will be implanted targeting the dorsal lateral geniculate nucleus (dLGN). (illustration needed)

2.3 Engineered directional neural networks

It is well established that the connectivity within biological neural networks is a major determinant of the emerging electrophysiological dynamics. For example, the microcircuit of the cat visual cortex exhibits a high degree of sparsity with predominantly local inhibitory-, and excitatory connections to achieve its output (Douglas and Martin 1991). Despite the general agreement on the significance of neural circuits, the vast majority of in vitro models remain limited to random connectivity schemes. Neglecting this property of in vivo neural networks may be well justified in studies that focus on basic biological properties, for example in response to drug admission. However, any model system investigating higher level functional properties emerging at the circuits-level (e.g. learning mechanisms) requires confined connectivity.

More elaborately controlled connectivity schemes are indispensable for technology relying on living neural circuits. Biohybrid interfaces as described above rely fundamentally on directional connectivity. Innervation of neighboring RGC source wells may result in activity dynamics independent of the imposed electrical stimulation pattern, rendering single stimulation channels or the entire device unusable. For this reason it is crucial for viable biohybrid implants to achieve high degrees of growth directionality. Likewise, more sophisticated models focusing on functional aspects of the peripheral nervous system (PNS) may benefit from directional in vitro models. PNS circuits generally show a pattern where sensory-, or motor axons converge to form a nerve that eventually diverges again in the target location. Building an in vitro platform resembling this architecture would be extremely useful for studying neuropathy, traumatic nerve injury, tissue reinnervation and [neurapraxia, axonotmesis, neurotmesis ?], and the effects of nerve stretching. The canonical design of the biohybrid implant where multiple RGC source nodes converge into a common output channel replicates this motif.

The challenge of achieving directional in vitro networks is often reduced to imposing axonal or dendritic growth constraints once the neurons are seeded. Although it is conceivable that initially randomly connected neural networks develop directional connections solely by an electrically imposed activity pattern (Markram et al. 1997), this approach has so far been to no avail. Therefore, various in vivo inspired approaches have been taken to instead induce control on axonal outgrowth. Axon guidance mechanisms in vivo rely, broadly speaking, on two categories of cues: mechanical and chemical ones (Weiss 1941, Goodman et al. 1984). Chemical cues have been employed for guidance by integrating substrate surface modifications favoring certain growth paths. Although many attempts are limited to micro patterning with PDL falling short of the highly complex chemical micro environment observed in vivo, still, a notable degree of axonal growth control is achieved (Yamamoto et al. 2016). While chemical guidance remains a promising direction for engineering defined neural networks in the future, mechanical guidance has shown more promising results at larger network scales (Forró et al. 2018).

The idea of utilizing mechanical growth guidance in vitro is largely based on advances in microfluidics for neuroscience (Millet and Gillette 2012, Neto et al. 2016). These platforms are commonly fabricated from Polydimethylsiloxane (PDMS), a polymer that can be molded at high resolution using soft lithography, while also exhibiting acceptable biocompatibility properties (Millet et al. 2007). 3D mechanical guidance principles are based on the inertia of growing axons, e.g. the inability to grow in sharp turns, and the tendency of axons to attach to edges (Francisco et al. 2007). These two findings are the basis of

numerous PDMS design motifs proposed in the literature to achieve directional growth through PDMS micro structures: barbed-, and narrowing channels, (Feber et al. 2015, Peyrin et al. 2011,) redirecting hooks and consecutive arches (Pirlo et al. 2011, Na et al. 2017, Renault et al. 2016, Holloway et al. 2019), and diode-like triangles (Gladkov et al. 2017, Isomura et al. 2015). So far, the most competitive multi node directional networks are based on a relatively simple motif, where axons detachment from sharp radii prevents growth in the undesired direction (Forró et al. 2018).

While Forró et al. 2018 presented respectable results for four-node-networks, the nerve model system and surely the biohybrid implant require an order of magnitude more nodes, while also deviating from the rather simple one-to-one connectivity scheme. In this work we present a high resolution screen on the growth directionality in twenty many-to-one PDMS designs. . . .

2.4 Multiple object tracking

In this work, we employ a custom build, machine learning-based growth cone tracking model to screen PDMS micro structures for directional growth. Previous work has relied on screening network directionality electrophysiologically (Forró et al. 2018, Isomura et al. 2015, Feber et al. 2015), through calcium indicators (Na et al. 2017), manual-, or segmentation based axon counting (Pirlo et al. 2011, Forró et al. 2018) and by calculating fluoresce intensity ratios (Renault et al. 2016, Na et al. 2017). Due to the general geometrical complexity and the multitude of junctions within our micro structure designs, previously employed anatomically-based screening methods did not meet our requirements. Alternatively, functional screening methods can offer high resolution, yet they are often limited to low experimental throughput. For those reasons, we resorted to tracking growth cones during the initial outgrowth phase, yielding a high resolution, anatomically-based estimation of directionality.

The problem of multiple object tracking (MOT) consists of identifying objects and linking their identities over multiple video frames, either offline with the entire sequence available, or online/ causally where future frames are not observed. Extensions of this include the classification and segmentation of identified objects. With notable exception Braso and Leal-Taixe 2019, this problem has been divided into object detection and object association. Since the seminal paper by Krizhevsky, Sutskever, and Hinton 2017 introducing the concept on learned convolution kernels, object detection has been increasingly dominated by machine learning based detectors. While the architecture of an image classifier is straight forward, mapping from the image pixel map to the number of classes, object detection deals with an unknown number of instances within an image, making it unclear what the network output shape should be. The first solution to this problem was the recurrent convolution neural network (R-CNN) architecture by (citation), implementing the recurrent classification of small image regions (for improved versions see (Girshick 2015, Ren et al. 2015)). The inherently low inference speed in these architectures was addressed by the *you only look once* (YOLO) architecture by dropping the recursive aspect completely (Redmon et al. 2015, Redmon and Farhadi 2018, Long et al. 2020). The ensuing step of data association has been dominated by non machine learning based methods (Bewley et al. 2016, Kuhn 1955, Wang, Wang, and Yu 2019), although deep learning alternatives have recently been proposed as well (Wojke, Bewley,

and Paulus 2017, Yoon et al. 2019).

In the biological microscopy literature, the above is often found under the term *particle tracking*, indicating the focus on small objects such as cells, organelles, or proteins (Tsai et al. 2019, Anjum and Gurari 2020, Welshans and Bassell 2011). Although the general problem matches the outline above, tracking of biological objects, including growth cones, involves a specific set of additional problems. Concretely, the setup used for screening PDMS micro structures imposed the following challenges. (i) Objects of interest, i.e. growth cones are often extremely small, thus conventional CNN architectures based on hierarchical feature extraction of larger objects are not suitable. (ii) Microscopy images are taken at very high resolution, raising computational considerations. (iii) Inter frame intervals are long, here around 30 minutes, (iv) Growth cone appearance is highly variant; growth cones can overlap and collapse abruptly. (v) No labelled dataset exists, and widely available pretrained models generalize poorly. Our tracking implementation is build on established methods with modifications addressing the points i-v. For more details see methods 3.2.5.

3 Methods and Materials

3.1 Experimental procedures

3.1.1 Dish preparation

First, WillCo glass dishes (\varnothing 30 mm, WillCO Wells) were rinsed with acetone, isopropanol and ultra pure Water (Millipore Milli-Q System, 18M Ω), then dried with a nitrogen gun. Next, double sided adhesive (DSA) rings were used to attach WillCo glass dishes to polystyrene dish frames. The assembled dishes were placed in a larger plastic dish with tape stripes preventing surface adhesion between dishes.

3.1.2 Poly-D-Lysine & laminin coating

The assembled glass dishes were coated using 1 ml Poly-D-Lysine (PDL) solution, incubating for 1-2 hours at room temperature. The solution was prepared using 1 ml of thawed up PDL stock (P7280, Sigma-Aldrich), and 8 ml of phosphate buffered saline (PBS) (10010015, Gibco, Thermo Fisher Scientific, Switzerland). After incubation, the PDL solution was removed and the dishes were washed 2 times with PBS, and once with deionized (DI) water.

Subsequent to PDL application, dishes were coated with 10 μ g/ml laminin. This solution was prepared by slowly thawing 50 μ l aliquots on ice, then adding 5 ml of NeurobasalTM plus (A3582901, Gibco). Between 300-800 μ l laminin solution was applied to cover the whole surface of the glass dish. After 24h incubation at 37 °C, laminin solution was removed and the dishes were washed 1 time with PBS, and 2 times with DI water.

Component	Volume [ml]	Stored at [°C]
Neurobasal Plus (Gibco, A3582901)	237.5	4
DMEM (Gibco 11960)	237.5	4
Glutamax	5	4
Sodium Pyruvate (100mM, Gibco 11360-070)	5	4
Antibiotic-Antimycotic (100x, Gibco 15240096)	5	-20
N2 Supplement	5	-20
B27+ (50x)	10	-20
N21 Supplement (50x, R&D Systems AR008)	10	-20
NAC Stock (5 mg/mL)	0.5	-20
Forskolin Stock (4.2 mg/mL)	0.5	-20
BDNF Stock (50 µg/mL, Preprotech 450-02)	0.5	-20
CNTF Stock (10 µg/mL, Preprotech 450-13)	0.5	-80
NGF 7S Stock (10 µg/mL, final 10 ng/mL)	0.5	-80
GNDNF (10 ng/mL)	0.5	-20

Table 1: RGC medium composition. This medium was used throughout for culturing RGC neurons.

3.1.3 PDMS micro structure design, fabrication & mounting

PDMS micro structures were designed in a multi stage computer aided design (CAD) process. This was necessitated by the vast number of design motifs investigated in this study. Although not primarily intended for 2D CAD, Fusion360 (Autodesk, San Rafael, California) was used in the initial design stage. Fusion360 was chosen because of its powerful version control and design history system, enabling the natural integration of design variables into the CAD workflow. More concretely, specific elements in different PDMS designs were inserted as separate components such that they could be updated independently from the base designs; for example the commonly used 2-joint motif. Single PDMS designs were then exported as .dxf files by projecting extruded bodies to 2D sketches. Importantly, the projection link had to be deleted to export valid .dxf files. The single PDMS designs were imported to AutoCAD (Autodesk, San Rafael, California) to define fabrication mask layers and arrange designs on the wafer. Finally, the wafer design was exported as a .dxf file and imported from KLayout where the final .gds2 file was generated. The wafer and PDMS designs were fabricated by Wunderlichips (Switzerland) employing standard soft lithography (for details see Forró et al. 2018).

The PDMS membrane delivered by Wunderlichips was separated into independent PDMS structures on a laser cutter (Speedy300, Trotec, Switzerland) using 8 % power at 14 cm/s. Subsequently, the structures were thoroughly rinsed with 70 % ethanol. For a subset of experiments, a PDMS frame was laser cut from 5mm thick cured PDMS. Using uncured PDMS, it was attached on the micro structure to enclose the output channel area. After curing for 1h at 80°C, they were picked up with a pair of surgical forceps and slowly placed on the coated glass dishes (see above). Importantly, a thin film of DI water was put on the glass dishes to facilitate mounting without enclosed air bubbles. As the last dish preparation step, RGC medium (see composition in Table 1) was added and the dishes were desiccated for 30-60 minutes to remove air from the PDMS micro channels.

3.1.4 Spheroid creation

pass

3.1.5 Primary Cell Culture (EYLUL)

All cell culture experiments were performed using primary cells from cortices and eyeballs of E18 embryos of time-mated pregnant rats (Janvier Laboratories, France). Animal experiments were approved by the Cantonal Veterinary Office Zurich.

3.1.6 Retina Dissections (EYLUL)

Dissection instruments, microscalpels, scissors and forceps were sprayed with 70 % ethanol prior to dissections. The retina dissections were performed under a benchtop microscope (DFC420C with 4X magnification, Leica, Germany) in a Petri dish filled with hibernate medium. Retinas were dissected out from whole eyeball. Firstly, all the tissue around the eyeballs was removed. The eyeballs were pinched along the cornea-sclera edge and cornea with forceps on both sides and gently pulled apart to cut open and isolate the retina. After gently removing the lens, the retina was later cut into square explants of around size 500 μm X 500 μm . After the dissections, the 100 μL dissected retina explants were transferred to a small Eppendorf tube and tagged with an adeno-associated virus (AVV) encoding for the mRuby virus (scAAV-DJ/2-hSyn1-chl-mRuby3-SV40p(A)). To do so, mRuby virus vial was thawed on ice and 1 μL was added to the explants. The explants were incubated with mRuby on ice for 1 hour.

3.1.7 AggreWell™ Preparation and Cell Dissociation (EYLUL)

AggreWell™ plate preparations to produce reproducible spheroids and cell dissociation were performed in parallel. AggreWell™ 800 microwell culture plates were prepared by adding 500 μL of AggreWell™ rinsing solution to the needed wells in order to prevent cell adhesion and promote spheroid formation. The plate was then balanced by adding 300 μL of DI water to each well of a standard well plate and centrifuged at 2000 x g for 5 minutes. The plate was examined under the microscope and check for bubbles. If there are trapped bubbles in the micro-well, the centrifuge procedure was repeated again. Afterwards, the AggreWell™ rinsing solution was aspirated and each well was rinsed with 2 mL of warm Neurobasal medium. 1 mL of complete medium was added to each well and the plate was kept in the incubator until cell dissociation was completed. For the cell dissociation, firstly, PBG solution was prepared by mixing 50 mg BSA in 50 ml sterile PBS together with 90.08 mg glucose. In order to prepare the Papain solution, 2.5 mg Papain was added to 5 mL of PBG and vortexed. After allowing 30 mins for dissolving, the solution was sterile filtered using a 0.2 μm filter. Finally, 5 μl DNase was added. 5 ml Papain solution was added, mixed gently and incubated at 37 °C for 15min and was shaken gently every 5min. Papain solution was aspirated without disturbing the pellet and 5ml Neurobasal media supplemented with 10 % FBS was added. After waiting for 3 min, media was removed without disturbing the pellet. This wash step was repeated twice by adding 5 ml Neurobasal media, waiting 3 minutes and removing medium. Finally, 4mL Neurobasal Plus medium supplemented with B27+ and anti-anti was added for 8 cortices. The cortices were then pipetted up with a 5 mL Pipette boy and quickly ejected to dissociate the cells. The cells were strained using a 40 μm cell strainer and a cell count was performed using Trypan Blue and a hemocytometer. Once the viable

cell concentration was determined, concentration of the cell suspension was adjusted to determine the number of cells required to obtain 8000 cells per microwell based on the desired number of cells per microwell multiplied by 300 microwells per well. After adding the required volume of the cell suspension to the wells, complete medium was added to each well to have a final volume of 2 mL in each well. 1 μ L mRuby and with 0.5 μ L of the calcium indicator was added into each well(s) to transduce the cells. The medium in the wells were pipetted up and down to make sure cells were evenly distributed. AggreWellTM plate was balanced again and immediately centrifuged at 100 x g for 3 minutes to ensure that the cells were captured in the micro-wells. Even distribution of cells inside the micro-wells were confirmed under the microscope and the plate was incubated at 37 °C with 5% CO₂ for 24 hours before seeding to allow for the formation of spheroids.

3.1.8 Cell Seeding and Primary Neuronal Cell Culture (EYLUL)

Explant and spheroid seeding into the wells were performed under a benchtop microscope (DFC420C with 4X magnification, Leica, Germany). Virus tagged explants and spheroids were gently pipetted and transferred to the wells of the mounted structures. Microscalpels were later used to insert the explants or spheroids into the wells. After the seeding, a small petri dish (\varnothing 40 mm) was filled with 2 mL of sterile DI water supplemented with 5 % anti-anti and placed next to the culture dish in the big dish in order to minimise evaporation of the cell culture medium and prevent drying out of the structures. For the electrodes, a cover was placed on top of the PDMS ring. Finally, cell culture dishes were transferred to the incubator and kept undisturbed for 3 days at 37 °C , 5 % CO₂. A half-medium change was performed every 2 days by using RGC medium for retina explants and Neurobasal plus medium supplemented with B27+ and anti-anti for cortical spheroids.

3.1.9 Timelapse recording

Fast solid state storage media was used to prevent a frame rate bottleneck from an insufficiently fast network connection.

3.2 Data analysis

3.2.1 Timelapse datasets

This work incorporates three PDMS micros structure timelapse recordings that were acquired at different timepoints. Accordingly, the data used in this project is based on three experiments, where each experiment was performed with 8-14 rat embryos (compare ?? for details). One of the three timelapses was solely obtained for generating model training data, thus the presented results are based on two experiments with a total of 16-28 biological replicates. A summery of timelapse datasets is given in Table 2.

3.2.2 Initial timelapse processing

The proprietary .oir files produced by the CLSM were converted to three dimensional .tif files using Python's bioformats package, which relies on a java virtual machine implemented within the javabridge package. Additionally, .tif frame sequences were rendered to .mp4 video using scikit-image and open-cv (Suppl. Figure 1 A). These videos were used for initial evaluation of the timelapse, validating for example absence

	Acquired	Setup	T [min]	n frames	Length [days]	Model usage
Dataset1	20.12.20	1 designs	40	37	1	Training
Dataset2	27.08.21	2 designs, chamber	31	210	4.5	Training
Dataset3	27.10.21	18 designs, chamber	31	210	4.5	Inference
Dataset4	07.10.21	21 designs, stomachs	32	242	5.4	Inference

Table 2: Overview of timelapse recording data. *n designs* refers to the number of unique PDMS micro structure designs composing the dataset. *Chamber* setups employed large thalamic tissue pieces enclosed by a PDMS frame for concentrated attraction cues (see 3.1.3 for details). *Stomach* setups omitted PDMS frames and instead seeded a thalamic spheroid in the target well (see Figure 3 for stomach illustration). T refers to the temporal period of the recording. White space between rows indicates different experiments.

of undergrowth. The transmission channel of each PDMS micro structure timelapse was then loaded into napari, a python based n-dimensional image viewer (Sofroniew et al. 2021). Using `skimage.filters` to segment the micro channels in the PDMS designs, edge magnitude was detected with `prewitt()`, gaussian smoothing was performed with `gaussian()` ($\sigma = 1$), thresholding was done with `threshold_otsu()`, and finally, the segmentation was cleaned up using `skimage.morphology.binary_closing()` (diameter = 4) (Suppl. Figure 1 B). Subsequently, the segmentation of the PDMS micro channels was manually cleaned up, mainly using the bucket tool to fill areas enclosed by detected edges. To remove patches in the mask, the target point of the PDMS design was labelled and used as the origin to perform `skimage.segmentation.flood()`. As a last step, both the final output channel and the first 100 μm of the channels exiting the source wells were segmented and saved as binary masks (Suppl. Figure 1 C).

3.2.3 Axon growth cone labelling

The axon growth cone tracking model was trained using Dataset1, and Dataset2 which included timelapse recordings of three unique PDMS designs (compare Table 2). The labelling of these three image sequences was performed by one human expert using the napari image viewer (Suppl. Figure 2 A). The workflow for obtaining the four dimensional label of `FrameID - AxonID - X coordinates - Y coordinate` was as follows:

1. Load timelapse sequence.
2. Create empty set of axon identities.
3. Inspect short time slice of 3-6 frames for distinct, coherently moving blob.
4. Identify axon identity by its growth cone.
5. Trace axon identify over adjacent frames until unidentifiable.

In the scenario where two separate growth cones converge forming a single observable growth cone, one of the two identities was arbitrarily chosen to be continued while the other one was terminated. Hence, the underlying number of axons for a given growth cone label may be larger than one. It should also be considered that there is some degree of uncertainty in the ground truth labels. Especially when the PDMS micro channels become largely filled, distinguishing between GFP-protein trafficking along existing axons versus new growth cones becomes challenging. The annotations here were consistently done more conservatively, weighting the avoidance of false positives higher than missing true positives. Following this conservative labelling methodology, an axon identity was only

considered if it appeared over more than three frames. From three concatenated PDMS micro structure timelapses, 300 growth cones were identified over N=327 frames where the average axon identity lifetime was 24 frames. An overview of the identify lifetime is given in Suppl. Figure 2 B; four labelled example frames are shown in Suppl. Figure 3.

3.2.4 Timelapse data preprocessing

The CLSM 12bit gray scale intensity values saved as 16bit unsigned integers were first converted to a scale of 0 to 1 using `skimage.util.img_as_float()`. For image sequences that had an offset in the intensity profile, this offset was subtracted such that the minimal intensity was always 0. Next, the segmentation of the micro channels was used to mask the image sequence (see Suppl. Figure 1 C for example mask). The resulting initial distribution of intensity values for both training and inference data is shown in (Figure 1 A top left). In the next step, intensity values below threshold = 0.00083 were clipped and set to 0 (Figure 1 A top right). Next, the intensity profile I_{in} was stretched using `skimage.exposure.adjust_log()` function with a gain $g = 1$ which transformed the distribution according to formula 1 (Figure 1 A bottom left).

$$I_{out} = g * \log(1 + I_{in}) \quad (1)$$

Finally, the intensity distribution was divided by the global standard deviation across the entire training image sequence, ensuring unit variance in the model input data (Figure 1 A bottom right). Both frame-wise, and mean-related standardizations were omitted since their application resulted in decreased detection performance. The intensity distributions from train- and inference data do not overlap in Figure 1 A because the sparsity differs vastly across frames. Train intensity values do not increase from t_0 to t_N because t_N corresponds to a different timelapse video (Dataset2) which is more sparse than t_0 (Dataset1).

3.2.5 Growth cone detection model

3.2.5.1 Temporal context frames

The growth cone detection model implemented in PyTorch follows the general approach of YOLO (You Only Look Once) (Redmon et al. 2015) where the detections are obtained by a single pass through the network (Figure 1 B). The first aspect in which it deviates from the original is that instead of inputting an RGB image, the network receives a temporal stack of five gray scale images. Concretely, to detect growth cones at frame t_0 , frame $t_{-2}, t_{-1}, t_0, t_1, t_2$ are fed into the network. This architecture aims to imitate the strategy of human labelling: by inspecting single frames, growth cone identification is highly uncertain; only when scanning sequences of frames, coherently moving blobs of particular shape and dynamics can be linked to growth cones and thus an axon identity. To always provide full temporal context, frame t_0, t_1, t_{N-1}, t_N were omitted from detecting growth cones in the image sequence. Computing the motion between frames manually by subtraction yielded decreased detection performance over the implicit approach of passing temporal context frames. An illustration of the motion computation is shown in Figure 1 C.

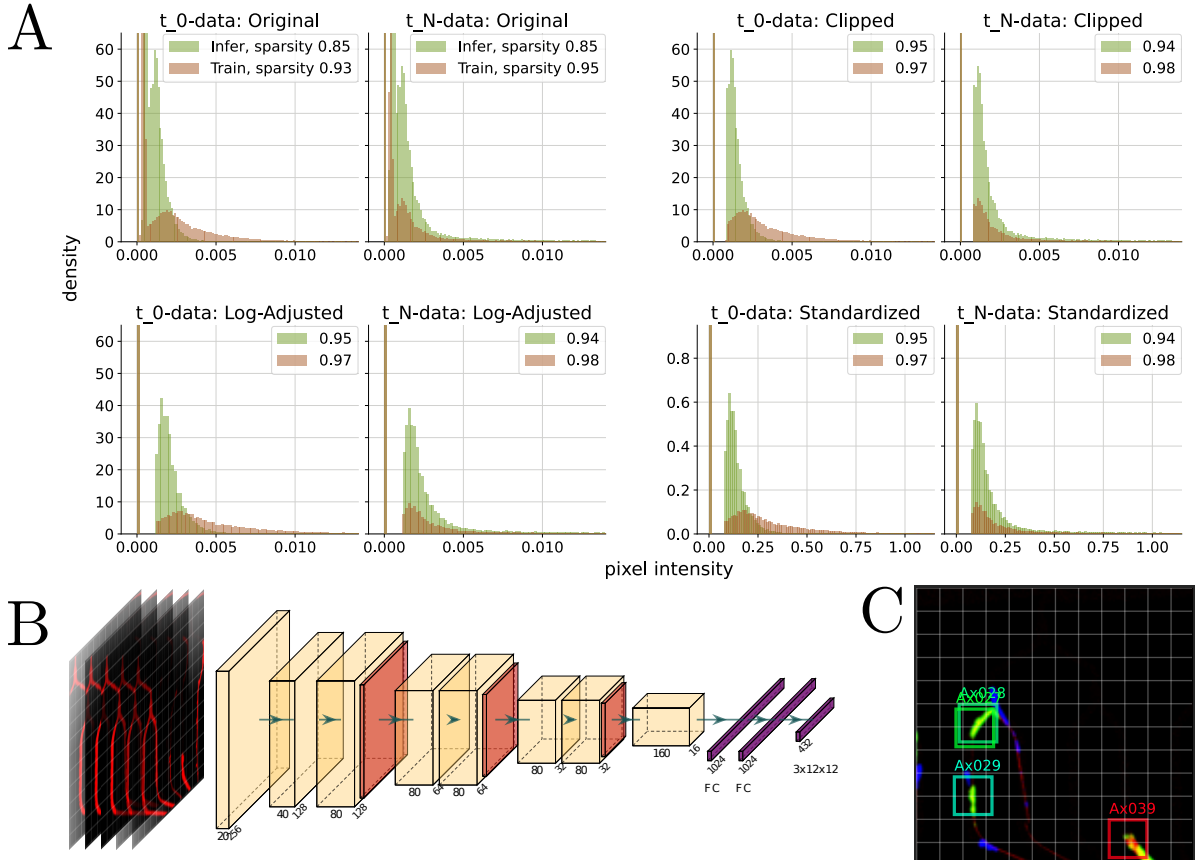


Figure 1: Growth cone detection model overview. **A** Pixel intensity distribution of training-, and inference data at t_0 and t_N over three major preprocessing steps. The two plots top left show the initial pixel intensity distributions, top right after clipping, bottom left after log adjusting, and bottom right after standardization. Histograms on the left were obtained from sampling 10^6 pixel values from the first frame, histograms on the right from the last respective frame. The inference data to produce the histograms (brown) was taken from a representative image sequence from Dataset3 (see Table 2). The number in the legend indicates the proportion of image values equal to zero (sparsity). Note that outlier intensity values are not shown. **B** CNN architecture. Each yellow block in represents a sequence of 2D-convolution, batch normalization (Ioffe and Szegedy 2015), and Leaky ReLU (Maas, Hannun, and Ng 2013). Orange layers stand for maximum pooling operations. FC stands for fully connected layers. **C** Example tile illustrating the YOLO label format. Each grid box can be predicted to contain a growth cone. In this example, 4 of 12 x 12 grid boxes are positive. Green colors in the tile represent positive motion (pixel intensity increased from frame t_0 to t_1), blue represents negative motion. Grid box size = $26 \mu\text{m}$.

3.2.5.2 Tiling

Each yellow block in Figure 1 B represents a sequence of 2D-convolution, batch normalization (Ioffe and Szegedy 2015), and Leaky ReLU (Maas, Hannun, and Ng 2013). Orange layers stand for maximum pooling operations. As performing detection on the original resolution of 3868 x 1972 was computationally intractable, the timelapse frames were split into 512 x 512 tiles (see Figure 1 C and grid in Suppl. Figure 3). The CNN computes a convolutional feature map of 16 x 16 x 160, thus a single *feature pixel* represents a region of $\frac{512}{16} = 32$ pixels in the original 512 x 512 input image. The CNN output resolution was a relevant consideration for its architecture, as the detection objects of interest are small and potentially locally clustered (using microscopy settings described in ??, growth cones are between 4-26 pixels). If the same CNN feature output resolution was to be achieved using original timelapse frames, the CNN output would be of shape of $\frac{3868}{32} \times \frac{1972}{32} \times 160 \approx 120 \times 61 \times 160$. Storing the weights between this high-resolution CNN feature map and the first fully connected layer exceeded GPU memory. An additional computational benefit is achieved by skipping empty tiles. From visual inspection, the discontinuities between tiles did not seem to result in decreased detection performance for growth cones near the tile edges.

3.2.5.3 Detection output format

Following the general YOLO label format, the network is trained to find a mapping from a single tile CNN feature map to a 12 x 12 x 3 array. Here, the first two dimensions represent a grid of the input tile, the last dimension refers to the confidence of the respective grid box containing a growth cone, and X-, Y grid box coordinates referring to the relative location of a growth cone within the box (Figure 1 C). This representation results in the limitation, that only one growth cone can be detected per grid box. As the example in Figure 1 C shows, close growth cones may still be detected as two separate identities if their centers are located in different grid boxes. In the worst case scenario, the spatial detection resolution of multiple growth cones is limited by the grid box size which is equal to $\frac{512}{12} = 43$ pixels or 26 μm . This resolution was sufficient for the application of our model as densely grouped growth cones were the exception.

To drop overlapping detections, non max suppression was applied to the final detection output according to (Bodla et al. 2017) using a minimum euclidean distance of 23 pixels.

3.2.5.4 Training procedure

The training data was split into 287 train frames (0.87), and 40 (0.13) consecutive test frames which spanned two different PDMS micro structures. The final model used for inference was trained on the entire dataset. Using translation, rotation, horizontal and vertical flipping as data augmentation, the model was trained up to convergence for 1000 epochs (Figure 2 A). The loss function below (2) is a slight modification from the original.

$$\lambda_{anchor} \sum_{i=0}^{S^2} \sum_{j=0}^B \mathbb{I}_{ij}^{obj} [(x_i - \hat{x}_i)^2 + (y_i - \hat{y}_i)^2] + \lambda_{obj} \sum_{i=0}^{S^2} \sum_{j=0}^B \mathbb{I}_{ij}^{obj} (c_i - \hat{c}_i)^2 + \lambda_{noobj} \sum_{i=0}^{S^2} \sum_{j=0}^B \mathbb{I}_{ij}^{noobj} (c_i - \hat{c}_i)^2 \quad (2)$$

where $S = 12$ is the number of tiles, $B = 1$ is the number of detections per grid box, \mathbb{I}_{ij}^{obj} equals to 1 if a growth cone exists, 0 otherwise, \mathbb{I}_{ij}^{noobj} equals to 0 if a growth cone exists,

1 otherwise, c_i refers to the confidence that an object exists in the grid box, and x_i, y_i represent the grid box coordinates. $\hat{\cdot}$ stands for the ground truth label. The loss terms for predicting coordinates, object presence, and object absence are weighted according to $\lambda_{anchor} = 45$, $\lambda_{obj} = 54.25$, and $\lambda_{noobj} = 0.75$ respectively. The balancing of those terms is based on the proportion of positive grid boxes which is $\approx 0.7\%$. The initial learning rate was set to 0.0005 and decayed with a rate given in formula 3.

$$\gamma = e^{-\frac{1}{10}\sqrt{x}} \quad (3)$$

where γ is multiplied with the original learning rate, and x refers to the current epoch. Pytorch's Adam optimizer (Kingma and Ba 2014) was used for fitting the model with $\beta_1 = 0.9$, $\beta_2 = 0.999$.

3.2.5.5 Data association

The implemented growth cone tracking model follows a classical object tracking paradigm of splitting the problem into object detection and identity association. For this second step, the detections produced by the YOLO-like architecture need to be classified into unique growth cone identities that live over several video frames. In this work, identity assignment is framed as a graph problem where we seek minimum cost flow solutions (Wang, Wang, and Yu 2019). At a high level, nodes represent detections at particular frames, and edges represent identity associations between them (see illustration in Figure 2 E). Each detection confidence is also represented as an edge, which elegantly incorporates the detection model uncertainty into forming identity trajectories through the graph and avoids the setting of explicit detection confidence thresholds. At the basis of associating detections between frames is the cost we assign between them. This cost can be interpreted as the likelihood the two detections correspond to the same growth cone identity. In contrast to other domains where visual similarity is highly relevant, the edge costs here are completely based on the spatial distance between detections. Specifically, the A* distances (Hart, Nilsson, and Raphael 1968) between them computed on the segmented PDMS micro channel mask. This cost considers the constraint, that growth cones can only translocate within the micro channels and are limited in outgrowth speed. Solving the graph optimization problem includes the constraint, that a node can only receive and emit a single edge, or in other words, a node can only represent a single identity. As shown by Wang, Wang, and Yu 2019, the graph can be solved optimally and efficiently using integer linear programming. The implementation here is based on the open-source package `libmot`, using the build-in `MinCostFlowTracker`. The optimal hyperparameters listed and explained in table 3 were identified with a grid-search algorithm on test data (see Figure 2 D).

3.2.6 Directionality inference from tracking

Using the growth cone trajectories obtained from the model, the degree of directional growth through the PDMS micro structures can be inferred. Analogous to the identity association cost employed for formulating the graph, directionality inference also relies on computing A* paths on the micro channel segmentation mask. For each detection that composes the growth cone trajectory, we compute the shortest distance to a human-labelled target point located in the output channel (see Suppl. Figure 1 C). Our PDMS designs have the property, that the shortest path towards this point is precisely the desired growth path. More intuitively, the desired growth path towards the output channel has

Edge cost threshold	Entry-exit cost	Miss rate
0.7	2	0.6
Maximum number of misses	Minimum network flow	Maximum network flow
1	5	450
Visual similarity weight	Confidence capping method	
0	<i>scale</i>	

Table 3: Minimum cost flow hyperparameters. The edge cost threshold determines if an edge is pruned or kept, the entry-exit cost defines the cost of creating and terminating identities, the maximum number of misses indicates for how many frames an identity can be not detected, but still not terminated, the miss rate determines how much cost is incurred from missing detections (low means high cost), minimum and maximum network flow gives the minimum and maximum number of identities over all frames, visual similarity weight determines the degree to which visual similarity between detections contributes to the cost, and finally the confidence capping method sets the behavior for confidence values above 1, where *scale* means normalize to maximum confidence.

no detours. Thus, we can employ the A*-shortest path towards the output channel as a proxy for confirming the correct growth direction through the micro channels. Concretely, a correctly growing axon should exhibit constantly decreasing A* distances towards the output channel. Conversely, any increase in distance indicates growth in the undesired direction.

3.2.7 Directionality evaluation metric

A variety of metrics could be considered for evaluating the degree of directional growth through PDMS micro structures. At the basis, metrics rely on the distance towards the output channel as explained above. An example of these distances in a particular time-lapse is shown in ???. We considered comparing the number of axons with negative,- and positive average slopes, as this would indicate the number of correctly,- versus incorrectly growing axons, respectively.

We need to consider the biases of each metric. Given that structures join at different locations, you get an inherent advantage for those that join late.

growth speed is lower in more complicated designs, benefit from the metric above

metric that combines reached target, reached neighbour and directionality? Correct dir 1 point, reached goal 5? Arbitrary weighting....

median vs mean gives very different story. argue for mean as outliers matter

v5 has reached neighbour, reached target, v6 has directions data

Speed and stagnation results

We chose metric...

3.2.8 Statistics

3.2.9 Between dataset variance

4 Results

4.1 Tracking performance

—Motivation why we build it—

The presented model splits the tracking problem into growth cone detection and identity association. A representative example of detections is shown in Figure 2 B. Given the temporal stack of five image tiles, the detection model accurately identifies growth cones in PDMS micro structure timelapse frames. False positive detections made by the model are often ambiguous image regions that may be interpreted as positives under less conservative ground truth labelling. On the test set, the detector reaches a precision of 0.73, and recall of 0.79. F1 score at a confidence threshold of 0.79 is 0.76 (Figure 2 C). A both deeper and wider CNN architecture did show decreased performance. The ensuing step of identity association was performed in a graph framework optimizing for minimum cost flow solutions. Matching detection performance in tracking is challenging as in addition to detection, identity switches, object occlusions, and suitable identity creation-, and termination need to be considered. Using the multiple object tracking benchmarks proposed in ??, our tracker achieves identity precision, recall and F1 score of 0.73, 0.68, 0.71, respectively, which is a reasonably small drop from detection performance (Figure 2 D). The commonly used MOTA (multiple object tracking accuracy) metric which considers the number of false positives, false negatives (including identity), and identity switches normalized to the number of ground truth labels was 0.61. A more intuitive measure of tracking performance is visualized by the top bar in Figure 2 D, indicating the proportion of growth cones mostly tracked (0.57), partially tracked (0.23), and mostly lost (0.2).

Although not utilized for our application of the tracking model, axons can be reconstructed from the growth cone track, assuming that outgrowth followed the shortest path between detections.

4.2 Micro structure designs

The tracking model described above was used for evaluating a set of 21 PDMS micro structures designed for directing axon growth from multiple sources towards a common target. These designs are the result of unpublished previous work extensively described in supplementary information 1 (also see for illustration of all designs). In short, the 21 designs test a set of presumably relevant variables that yield directional axonal growth, including different types of 2-joints, joint placements and joint frequencies. Figure 3 illustrates the specific features implemented in the collection of designs. Design 05 on the right exemplifies the general PDMS architecture composed of four source wells, the convergence lane, the higher output channel with added diffusion wells and finally a target stomach (Forró et al. 2018).

micro strcoutures , design features introduce basic tracking results: tracking plot base subtr and normal show speed and varaince plots split by dataset (SF?) and describe between dataset varaince

speed higher in small channels

Optional; show n good trans. n bad transision statistical analysis

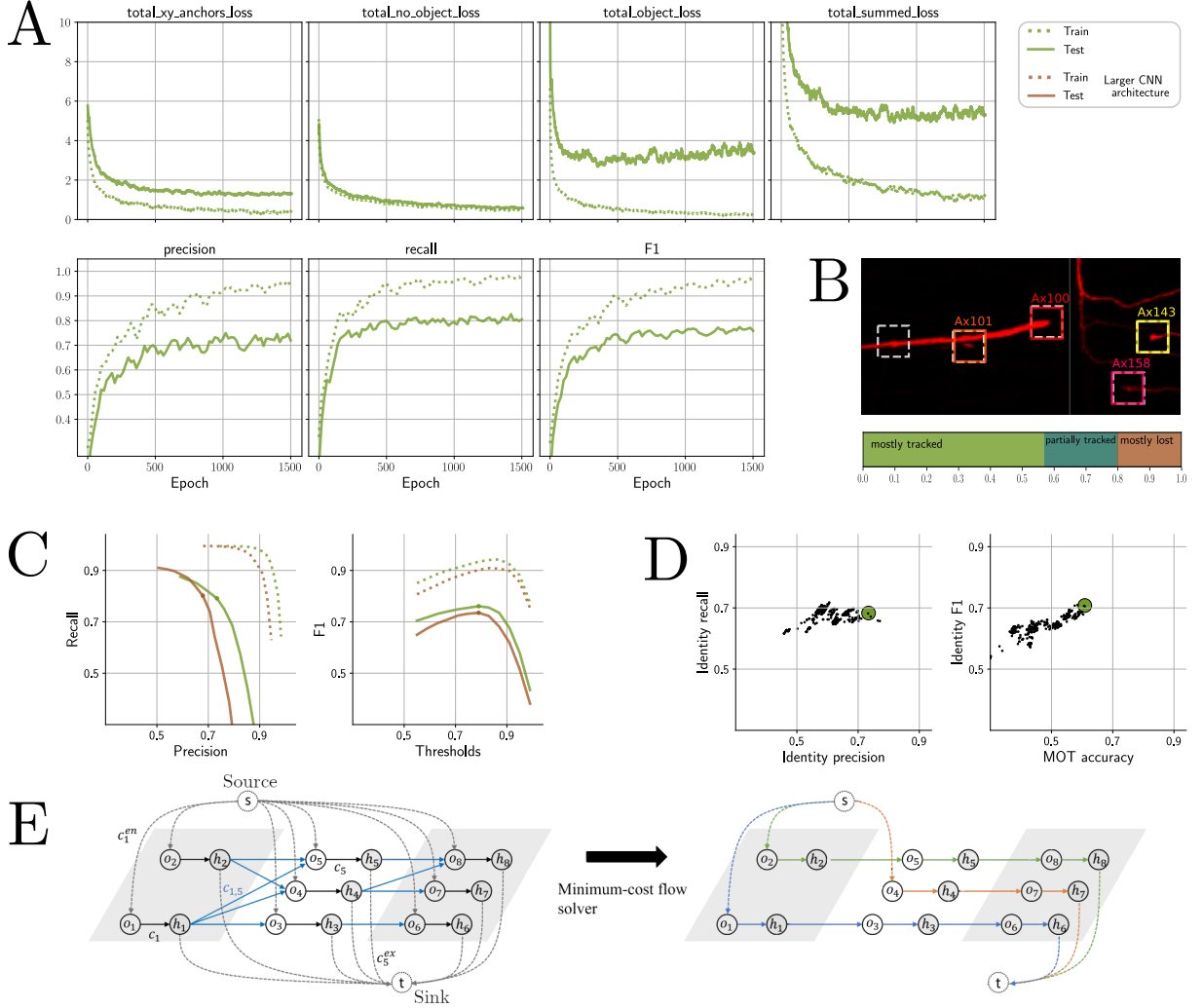


Figure 2: Growth cone tracking model performance. **A** Loss and performance over 1500 training epochs. Dotted line refers to train set, solid line to test. The plotted loss was smoothed with an exponentially decaying kernel over 25 epochs, precision, recall, and F1 over 60 epochs. **B** Representative growth cone detection example. Dashed boxes are predicted, colored ones are ground truth. Scale bar = 90 μm . **C** Detection performance. The maximum F1 score for varying confidence thresholds on test set is indicated by the dot. The brown line shows performance for a model with wider and deeper architecture. Legend in A applies. **D** Model growth cone tracking performance. Identity precision and recall incorporate classification of correct identity. Each black dot represents the performance using one set of hyperparameters, the green dot represents the highest scoring set (see Table 3) where identity F1 was 0.71, MOT accuracy 0.61. MOT accuracy measures the number of false positives, false negatives, and identity switches normalized to the number of ground truth labels. The top bar visualizes the proportion of growth cones that were mostly tracked (green, >80% identity lifetime tracked), mostly lost (brown, <20%), and partially tracked (dark green, between 20-80%). **E** Minimum cost flow optimization illustration adopted from (Wang, Wang, and Yu 2019). Frames are illustrated in gray and white background, detections within a frame are represented by a pre- (o_i), and post (h_i) node. Blue edges on the left represent costs between detections in adjacent frames. Coloured edges on the right indicate identity associations after solving the graph.

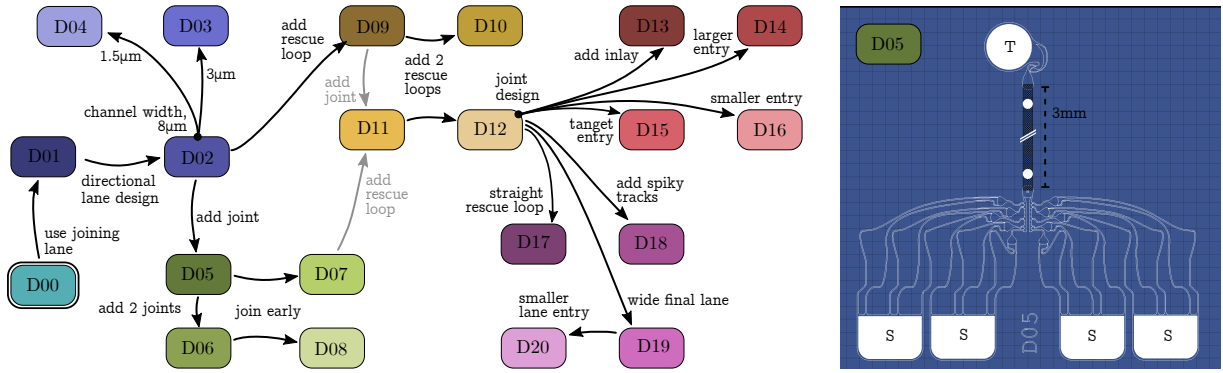


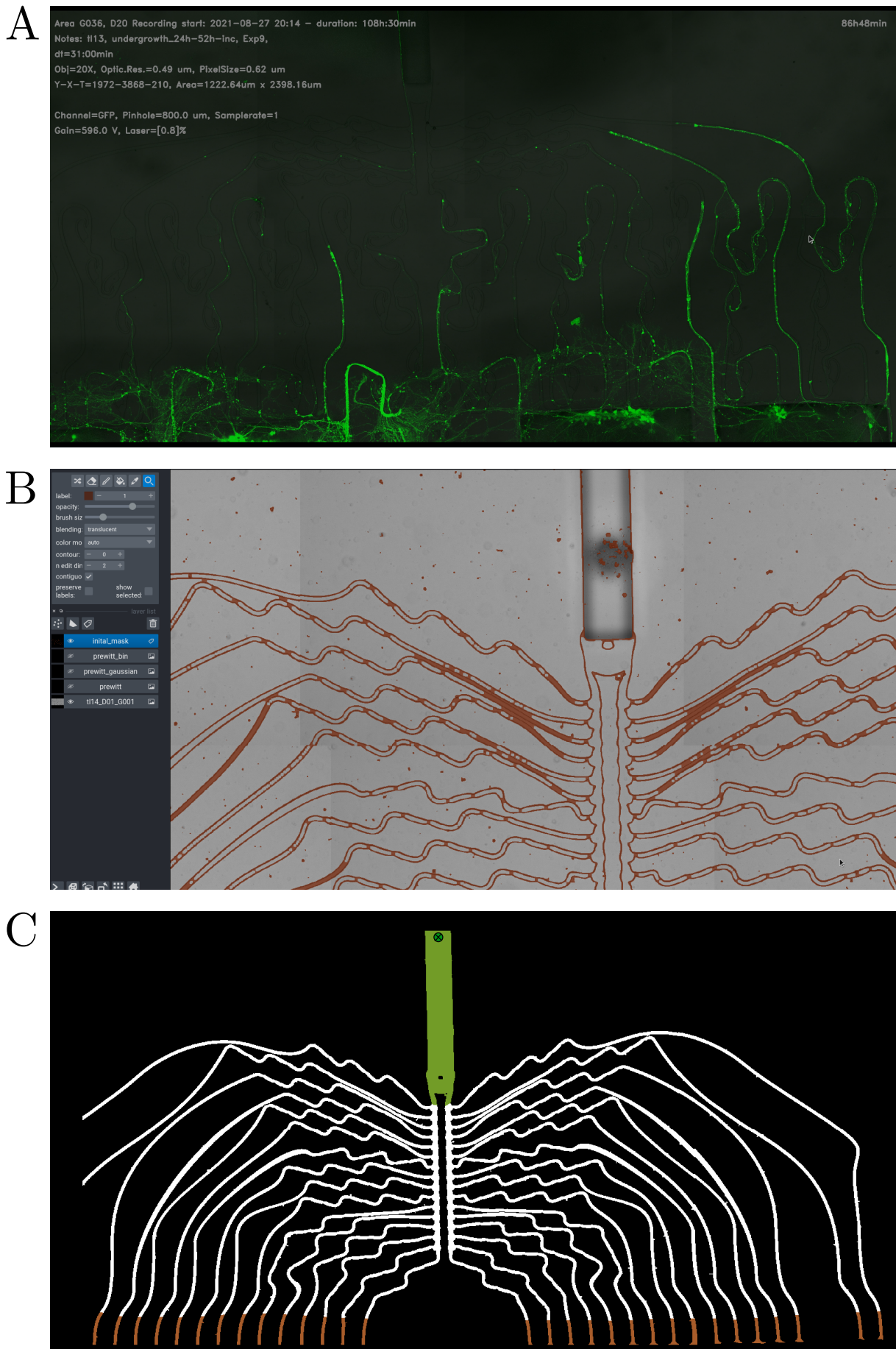
Figure 3: PDMS micro structure designs. The left illustration provides an overview of the 20 modelled micro structures including their distinguishing design features. Starting from design 0 (D00), the arrows can be interpreted as an implemented design change. For example, D05 and D06 differ specifically in the number of 2-joints. On the right, the D05 design is shown as an example. Filled white regions are openings, white lines indicate 6 μ m high channels, the black region represents the 75 μ m high output channel (note discontinuity for illustrative reason). RGC spheroids are seeded in the source wells (S), the thalamic attractor is placed in the target well (T). Grid dimension is 100 μ m.

show reached target/reached neighbour (no signf. differences)

5 Discussion

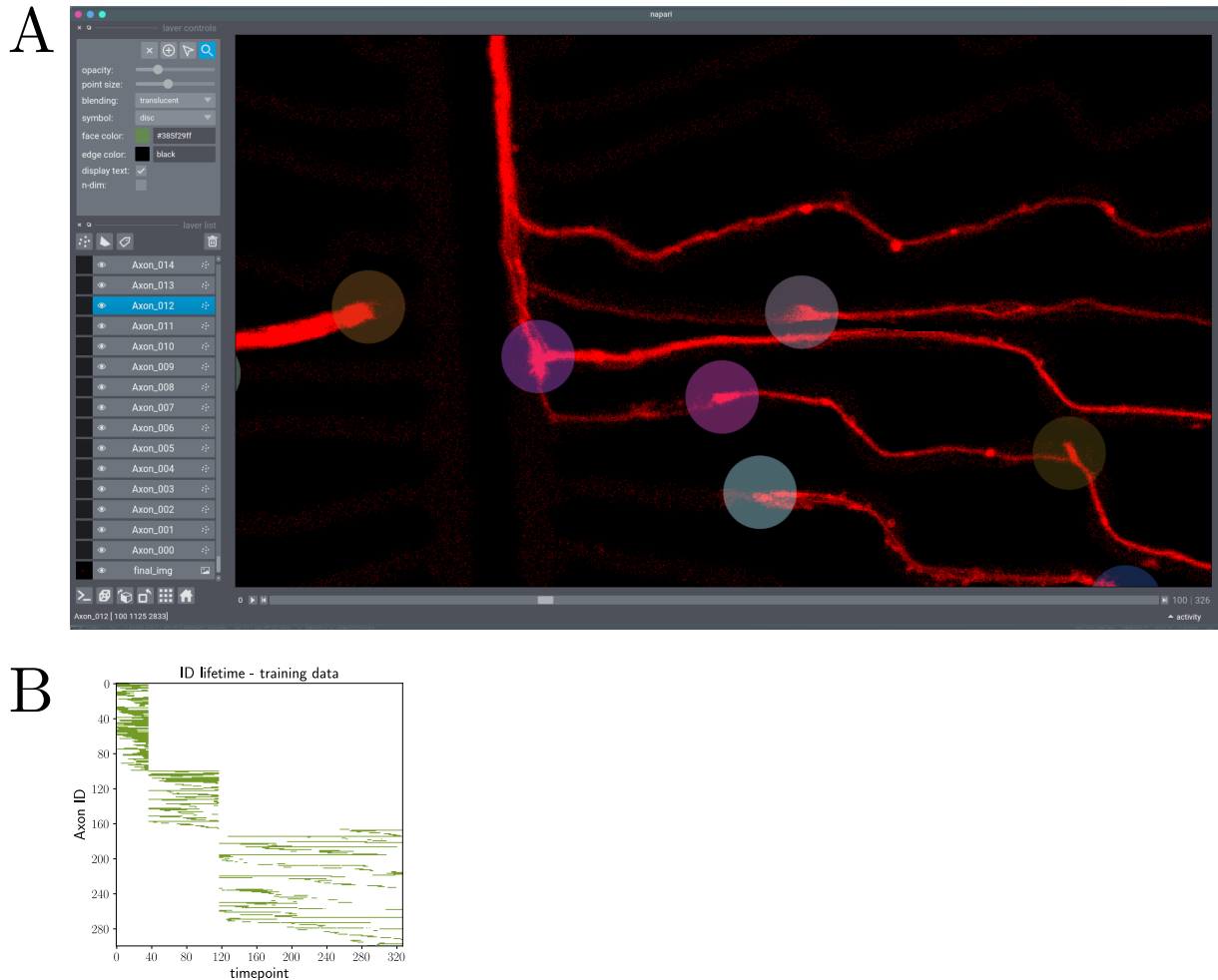
5.1 Model architecture and generalization

6 Supplementary Information

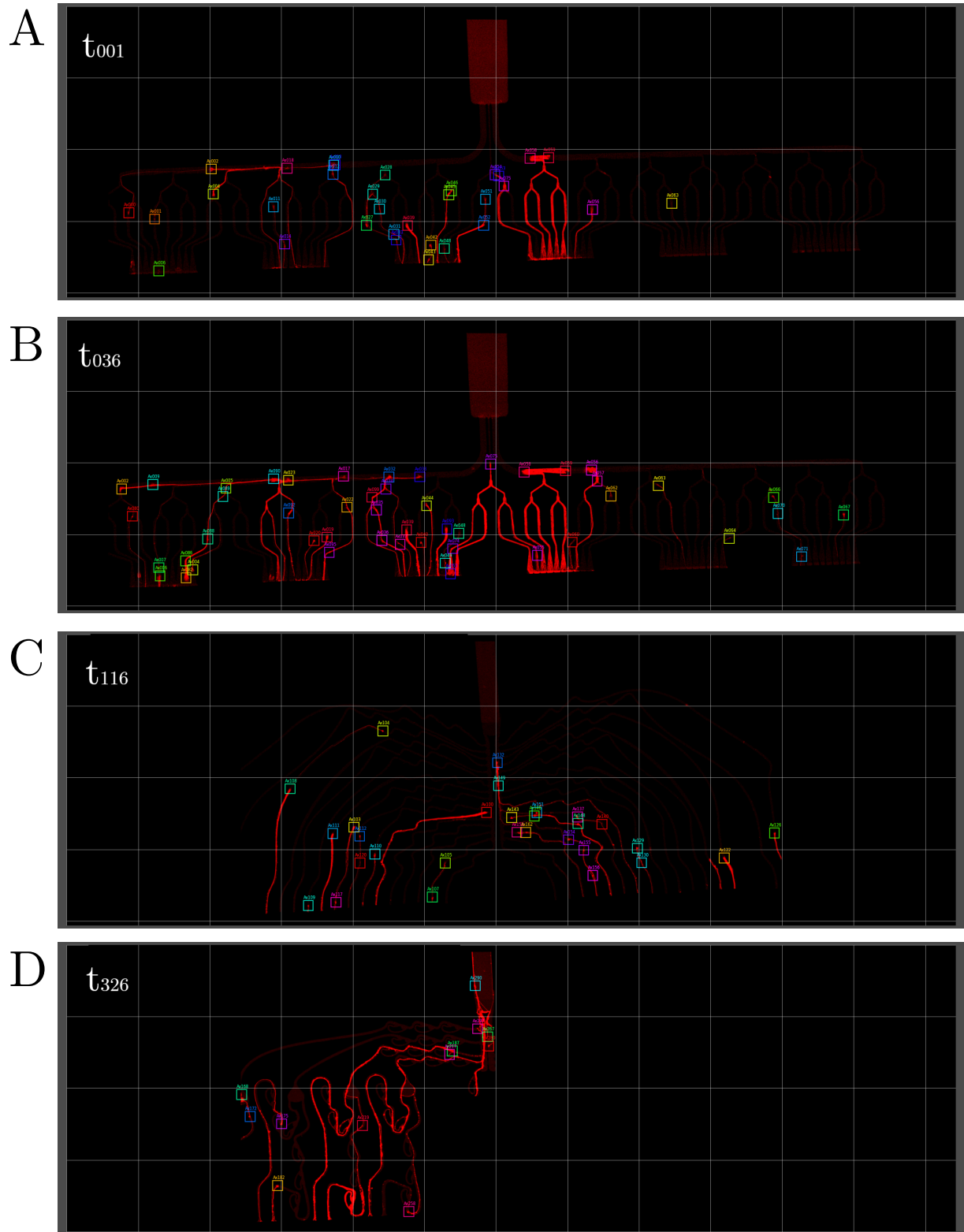


labelled and

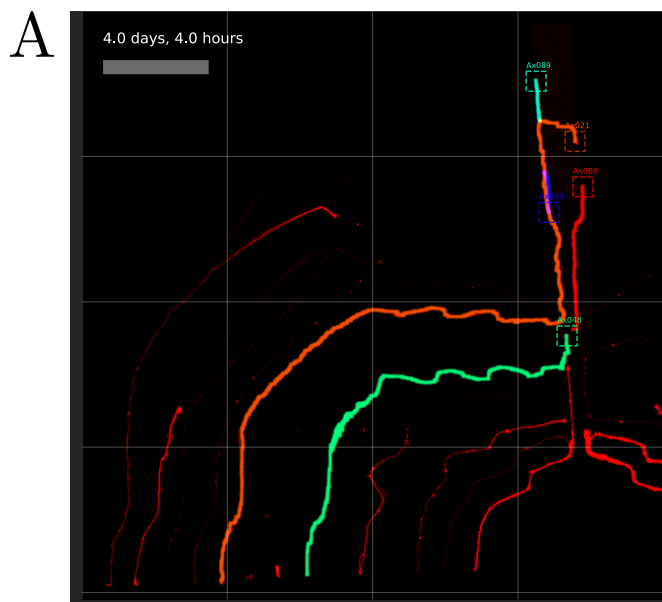
Supplementary Figure 1: Initial timelapse preprocessing steps. **A** A snapshot of the exported video including the relevant metadata of the recording. **B** The napari image viewer interface with the edge segmentation layer in brown. **C** The manually segmented binary mask of the micro channels in non-black, the output channel in green, and the exiting channels in brown. The green dot in the output channel marks the target point of the PDMS design.



Supplementary Figure 2: Axon growth cone labelling. **A** shows a snapshot of the napari image viewer during labelling. Each circle represents a growth cone label, the color corresponds to the identity. Each axon identity is saved as a napari-Points layer which are listed on the left. **B** illustrates the axon identify lifetime. A green point on this pixel map indicates that a label exists for the matching axon identity and frame. The three clusters originate from the concatenation of three PDMS microstructure timelapse videos.



Supplementary Figure 3: Labelled training data examples. **A** shows the first frame of the training data sequence. Each box represents a growth cone, the color indicates the identity over consecutive frames. **B** shows the last frame of Dataset1. **C** shows the last frame of Dataset2, PDMS micro structure 1 (compare Table 2). **D** shows the last frame of Dataset2, PDMS micro structure 2. Gridsize = 317 μm .



Supplementary Figure 4: Axon reconstruction from growth cone track. **A** For clarity, only a subset of identified axons is drawn.

References

- Mead, Carver (1989). *Analog VLSI Implementation of Neural Systems*. Ed. by Carver Mead and Mohammed Ismail. Vol. 80. Springer US. ISBN: 978-1-4612-8905-0. DOI: 10.1007/978-1-4613-1639-8. URL: <http://link.springer.com/10.1007/978-1-4613-1639-8>.
- Durand, Dominique M. (Sept. 2006). "What is Neural Engineering?" In: *Journal of Neural Engineering* 4 (4), E01. ISSN: 1741-2552. DOI: 10.1088/1741-2552/4/4/E01. URL: <https://iopscience.iop.org/article/10.1088/1741-2552/4/4/E01>
<https://iopscience.iop.org/article/10.1088/1741-2552/4/4/E01/meta>.
- Maynard, Edwin M., Craig T. Nordhausen, and Richard A. Normann (1997). "The Utah intracortical Electrode Array: a recording structure for potential brain-computer interfaces". In: *Electroencephalography and clinical neurophysiology* 102 (3), pp. 228–239. ISSN: 0013-4694. DOI: 10.1016/S0013-4694(96)95176-0. URL: <https://pubmed.ncbi.nlm.nih.gov/9129578/>.
- Jun, James J. et al. (Nov. 2017). "Fully integrated silicon probes for high-density recording of neural activity". In: *Nature* 2017 551:7679 551 (7679), pp. 232–236. ISSN: 1476-4687. DOI: 10.1038/nature24636. URL: <https://www.nature.com/articles/nature24636>.
- Stevenson, Ian H. and Konrad P. Kording (Jan. 2011). "How advances in neural recording affect data analysis". In: *Nature Neuroscience* 2011 14:2 14 (2), pp. 139–142. ISSN: 1546-1726. DOI: 10.1038/nn.2731. URL: <https://www.nature.com/articles/nn.2731>.
- Herrington, Todd M., Jennifer J. Cheng, and Emad N. Eskandar (Jan. 2016). "Mechanisms of deep brain stimulation". In: *Journal of Neurophysiology* 115 (1), pp. 19–38. ISSN: 15221598. DOI: 10.1152/JN.00281.2015/ASSET/IMAGES/LARGE/Z9K0011634190006. JPEG. URL: <https://journals.physiology.org/doi/abs/10.1152/jn.00281.2015>.
- Tong, Wei et al. (Mar. 2020). "Stimulation Strategies for Improving the Resolution of Retinal Prostheses". In: *Frontiers in Neuroscience* 14, p. 262. ISSN: 1662453X. DOI: 10.3389/FNINS.2020.00262/BIBTEX.
- Tresco, Patrick A. and Brent D. Winslow (2011). "The Challenge of Integrating Devices into the Central Nervous System". In: *Critical Reviews in Biomedical Engineering* 39 (1), pp. 29–44. ISSN: 0278-940X. DOI: 10.1615/CRITREVBIOMEDENG.V39.I1.30. URL: <https://www.dl.begellhouse.com/journals/4b27cbfc562e21b8,7d5e987c7e576915,1e61f79c5183ad8b.html>.
- Saxena, Tarun et al. (July 2013). "The impact of chronic blood-brain barrier breach on intracortical electrode function". In: *Biomaterials* 34 (20), pp. 4703–4713. ISSN: 01429612. DOI: 10.1016/j.biomaterials.2013.03.007.
- Grill, Warren M., Sharon E. Norman, and Ravi V. Bellamkonda (July 2009). "Implanted Neural Interfaces: Biochallenges and Engineered Solutions". In: <http://dx.doi.org/10.1146/annurev-bioeng-061008-124927> 11, pp. 1–24. ISSN: 15239829. DOI: 10.1146/ANNUREV-BIOENG-061008-124927. URL: <https://www.annualreviews.org/doi/abs/10.1146/annurev-bioeng-061008-124927>.
- Polikov, Vadim S., Patrick A. Tresco, and William M. Reichert (Oct. 2005). "Response of brain tissue to chronically implanted neural electrodes". In: *Journal of Neuroscience Methods* 148 (1), pp. 1–18. ISSN: 0165-0270. DOI: 10.1016/J.JNEUMETH.2005.08.015.

- Zemelman, Boris V. et al. (Jan. 2002). "Selective photostimulation of genetically chARGed neurons". In: *Neuron* 33 (1), pp. 15–22. ISSN: 0896-6273. DOI: 10.1016/S0896-6273(01)00574-8. URL: <https://pubmed.ncbi.nlm.nih.gov/11779476/>.
- Boyden, Edward S. et al. (Aug. 2005). "Millisecond-timescale, genetically targeted optical control of neural activity". In: *Nature Neuroscience* 2005 8:9 8 (9), pp. 1263–1268. ISSN: 1546-1726. DOI: 10.1038/nn1525. URL: <https://www.nature.com/articles/nn1525>.
- Mendoza, Skyler D., Yasmine El-Shamayleh, and Gregory D. Horwitz (May 2017). "AAV-mediated delivery of optogenetic constructs to the macaque brain triggers humoral immune responses". In: *Journal of Neurophysiology* 117 (5), pp. 2004–2013. ISSN: 15221598. DOI: 10.1152/JN.00780.2016/ASSET/IMAGES/LARGE/Z9K0051740960006. JPEG. URL: <https://journals.physiology.org/doi/abs/10.1152/jn.00780.2016>.
- Stieglitz, T. et al. (Aug. 2002). "A biohybrid system to interface peripheral nerves after traumatic lesions: design of a high channel sieve electrode". In: *Biosensors and Bioelectronics* 17 (8), pp. 685–696. ISSN: 0956-5663. DOI: 10.1016/S0956-5663(02)00019-2.
- Rochford, Amy E. et al. (Apr. 2020). "When Bio Meets Technology: Biohybrid Neural Interfaces". In: *Advanced Materials* 32 (15), p. 1903182. ISSN: 1521-4095. DOI: 10.1002/ADMA.201903182. URL: <https://onlinelibrary.wiley.com/doi/full/10.1002/adma.201903182> <https://onlinelibrary.wiley.com/doi/abs/10.1002/adma.201903182>.
- Purcell, E. K. et al. (Mar. 2009). "In vivo evaluation of a neural stem cell-seeded prosthesis". In: *Journal of Neural Engineering* 6 (2), p. 026005. ISSN: 1741-2552. DOI: 10.1088/1741-2560/6/2/026005. URL: <https://iopscience.iop.org/article/10.1088/1741-2560/6/2/026005> <https://iopscience.iop.org/article/10.1088/1741-2560/6/2/026005/meta>.
- Faveri, Sara De et al. (Apr. 2014). "Bio-inspired hybrid microelectrodes: A hybrid solution to improve long-term performance of chronic intracortical implants". In: *Frontiers in Neuroengineering* 7 (APR), p. 7. ISSN: 16626443. DOI: 10.3389/FNENG.2014.00007/BIBTEX.
- Tang-Schomer, Min D. et al. (Apr. 2014). "Film-Based Implants for Supporting Neuron-Electrode Integrated Interfaces for The Brain". In: *Advanced Functional Materials* 24 (13), pp. 1938–1948. ISSN: 1616-3028. DOI: 10.1002/ADFM.201303196. URL: <https://onlinelibrary.wiley.com/doi/full/10.1002/adfm.201303196> <https://onlinelibrary.wiley.com/doi/abs/10.1002/adfm.201303196> <https://onlinelibrary.wiley.com/doi/10.1002/adfm.201303196>.
- Adewole, Dayo O. et al. (Jan. 2021). "Development of optically controlled "living electrodes" with long-projecting axon tracts for a synaptic brain-machine interface". In: *Science Advances* 7 (4). ISSN: 23752548. DOI: 10.1126/SCIADV.AAY5347/SUPPLFILE/AAY5347_SM.PDF. URL: <https://www.science.org/doi/abs/10.1126/sciadv.aay5347>.
- Bourne, Rupert R.A. et al. (Feb. 2021). "Trends in prevalence of blindness and distance and near vision impairment over 30 years: an analysis for the Global Burden of Disease Study". In: *The Lancet. Global health* 9 (2), e130–e143. ISSN: 2214-109X. DOI: 10.1016/S2214-109X(20)30425-3. URL: <https://pubmed.ncbi.nlm.nih.gov/33275950/>.
- Tybrandt, Klas et al. (Apr. 2018). "High-Density Stretchable Electrode Grids for Chronic Neural Recording". In: *Advanced Materials* 30 (15), p. 1706520. ISSN: 1521-4095. DOI:

- 10.1002/ADMA.201706520. URL: <https://onlinelibrary.wiley.com/doi/full/10.1002/adma.201706520>
- Douglas, R. J. and K. A. Martin (Aug. 1991). "A functional microcircuit for cat visual cortex". In: *The Journal of physiology* 440 (1), pp. 735–769. ISSN: 0022-3751. DOI: 10.1113/JPHYSIOL.1991.SP018733. URL: <https://pubmed.ncbi.nlm.nih.gov/1666655/>.
- Markram, Henry et al. (Jan. 1997). "Regulation of synaptic efficacy by coincidence of postsynaptic APs and EPSPs". In: *Science* 275 (5297), pp. 213–215. ISSN: 00368075. DOI: 10.1126/SCIENCE.275.5297.213
- Yamamoto, H. et al. (July 2016). "Unidirectional signal propagation in primary neurons micropatterned at a single-cell resolution". In: *Applied Physics Letters* 109 (4). ISSN: 00036951. DOI: 10.1063/1.4959836.
- Forró, Csaba et al. (Dec. 2018). "Modular microstructure design to build neuronal networks of defined functional connectivity". In: *Biosensors and Bioelectronics* 122, pp. 75–87. ISSN: 0956-5663. DOI: 10.1016/J.BIOS.2018.08.075.
- Millet, Larry J. and Martha U. Gillette (Dec. 2012). "New perspectives on neuronal development via microfluidic environments". In: *Trends in neurosciences* 35 (12), pp. 752–761. ISSN: 1878-108X. DOI: 10.1016/J.TINS.2012.09.001. URL: <https://pubmed.ncbi.nlm.nih.gov/23031246/>.
- Neto, Estrela et al. (Nov. 2016). "Compartmentalized Microfluidic Platforms: The Unrivaled Breakthrough of In Vitro Tools for Neurobiological Research". In: *The Journal of neuroscience : the official journal of the Society for Neuroscience* 36 (46), pp. 11573–11584. ISSN: 1529-2401. DOI: 10.1523/JNEUROSCI.1748-16.2016. URL: <https://pubmed.ncbi.nlm.nih.gov/27852766/>.
- Millet, Larry J. et al. (2007). "Microfluidic devices for culturing primary mammalian neurons at low densities". In: *Lab on a chip* 7 (8), pp. 987–994. ISSN: 1473-0197. DOI: 10.1039/B705266A. URL: <https://pubmed.ncbi.nlm.nih.gov/17653340/>.
- Francisco, Herbert et al. (Aug. 2007). "Regulation of Axon Guidance and Extension by 3-Dimensional Constraints". In: *Biomaterials* 28 (23), p. 3398. ISSN: 01429612. DOI: 10.1016/J.BIOMATERIALS.2007.04.015. URL: /pmc/articles/PMC1952179//pmc/articles/PMC1952179/?report=abstract
- Feber, Joost Le et al. (2015). "Barbed channels enhance unidirectional connectivity between neuronal networks cultured on multi electrode arrays". In: *Frontiers in Neuroscience* 9 (NOV), p. 412. ISSN: 1662453X. DOI: 10.3389/FNINS.2015.00412/BIBTEX.
- Peyrin, Jean Michel et al. (Oct. 2011). "Axon diodes for the reconstruction of oriented neuronal networks in microfluidic chambers". In: *Lab on a Chip* 11 (21), pp. 3663–3673. ISSN: 14730189. DOI: 10.1039/C1LC20014C. URL: <https://pubs.rsc.org/en/>

- content/articlehtml/2011/1c/c1lc20014chhttps://pubs.rsc.org/en/content/articlelanding/2011/1c/c1lc20014c.
- Pirlo, R. K. et al. (Mar. 2011). “Biochip/laser cell deposition system to assess polarized axonal growth from single neurons and neuron/glia pairs in microchannels with novel asymmetrical geometries”. In: *Biomicrofluidics* 5 (1), p. 013408. ISSN: 19321058. DOI: 10.1063/1.3552998. URL: <https://aip.scitation.org/doi/abs/10.1063/1.3552998>.
- Na, Sangcheol et al. (Mar. 2017). “Microfluidic neural axon diode”. In: *Technology* 04 (04), pp. 240–248. ISSN: 2339-5478. DOI: 10.1142/S2339547816500102.
- Renault, Renaud et al. (June 2016). “Asymmetric axonal edge guidance: a new paradigm for building oriented neuronal networks”. In: *Lab on a Chip* 16 (12), pp. 2188–2191. ISSN: 14730189. DOI: 10.1039/C6LC00479B. URL: <https://pubs.rsc.org/en/content/articlehtml/2016/1c/c6lc00479bhttps://pubs.rsc.org/en/content/articlelanding/2016/1c/c6lc00479b>.
- Holloway, Paul M. et al. (Apr. 2019). “Asymmetric confinement for defining outgrowth directionality”. In: *Lab on a Chip* 19 (8), pp. 1484–1489. ISSN: 1473-0189. DOI: 10.1039/C9LC00078J. URL: <https://pubs.rsc.org/en/content/articlehtml/2019/1c/c9lc00078jhttps://pubs.rsc.org/en/content/articlelanding/2019/1c/c9lc00078j>.
- Gladkov, Arseniy et al. (Nov. 2017). “Design of Cultured Neuron Networks in vitro with Predefined Connectivity Using Asymmetric Microfluidic Channels”. In: *Scientific Reports* 2017 7:1 7 (1), pp. 1–14. ISSN: 2045-2322. DOI: 10.1038/s41598-017-15506-2. URL: <https://www.nature.com/articles/s41598-017-15506-2>.
- Isomura, Takuya et al. (Nov. 2015). “Signal transfer within a cultured asymmetric cortical neuron circuit”. In: *Journal of Neural Engineering* 12 (6), p. 066023. ISSN: 1741-2552. DOI: 10.1088/1741-2560/12/6/066023. URL: <https://iopscience.iop.org/article/10.1088/1741-2560/12/6/066023https://iopscience.iop.org/article/10.1088/1741-2560/12/6/066023/meta>.
- Braso, Guillem and Laura Leal-Taixe (Dec. 2019). “Learning a Neural Solver for Multiple Object Tracking”. In: *Proceedings of the IEEE Computer Society Conference on Computer Vision and Pattern Recognition*, pp. 6246–6256. ISSN: 10636919. DOI: 10.1109/CVPR42600.2020.00628. URL: <https://arxiv.org/abs/1912.07515v2>.
- Krizhevsky, Alex, Ilya Sutskever, and Geoffrey E. Hinton (May 2017). “ImageNet classification with deep convolutional neural networks”. In: *Communications of the ACM* 60 (6), pp. 84–90. ISSN: 15577317. DOI: 10.1145/3065386. URL: <https://dl.acm.org/doi/abs/10.1145/3065386>.
- Girshick, Ross (Apr. 2015). “Fast R-CNN”. In: *arXiv*. URL: <https://arxiv.org/abs/1504.08083>.
- Ren, Shaoqing et al. (June 2015). “Faster R-CNN: Towards Real-Time Object Detection with Region Proposal Networks”. In: *arXiv*. URL: <https://arxiv.org/abs/1506.01497>.
- Redmon, Joseph et al. (June 2015). “You Only Look Once: Unified, Real-Time Object Detection”. In: *Proceedings of the IEEE Computer Society Conference on Computer Vision and Pattern Recognition* 2016-December, pp. 779–788. ISSN: 10636919. DOI: 10.1109/CVPR.2016.91. URL: <https://arxiv.org/abs/1506.02640v5>.
- Redmon, Joseph and Ali Farhadi (Apr. 2018). “YOLOv3: An Incremental Improvement”. In: *arXiv*. URL: <https://arxiv.org/abs/1804.02767>.

- Long, Xiang et al. (July 2020). "PP-YOLO: An Effective and Efficient Implementation of Object Detector". In: *arXiv*. URL: <http://arxiv.org/abs/2007.12099>.
- Bewley, Alex et al. (Aug. 2016). "Simple online and realtime tracking". In: *Proceedings - International Conference on Image Processing, ICIP* 2016-August, pp. 3464–3468. ISSN: 15224880. DOI: [10.1109/ICIP.2016.7533003](https://doi.org/10.1109/ICIP.2016.7533003).
- Kuhn, Harold W (Mar. 1955). "The Hungarian Method for the Assignment Problem". In: *Naval Research Logistics Quarterly* 2 (1–2), pp. 83–97. DOI: [10.1002/nav.3800020109](https://doi.org/10.1002/nav.3800020109).
- Wang, Congchao, Yizhi Wang, and Guoqiang Yu (Nov. 2019). "Efficient Global Multi-object Tracking Under Minimum-cost Circulation Framework". In: *IEEE Transactions on Pattern Analysis and Machine Intelligence*, pp. 1–1. ISSN: 0162-8828. DOI: [10.1109/tpami.2020.3026257](https://doi.org/10.1109/tpami.2020.3026257). URL: <https://arxiv.org/abs/1911.00796v2>.
- Wojke, Nicolai, Alex Bewley, and Dietrich Paulus (Mar. 2017). "Simple Online and Real-time Tracking with a Deep Association Metric". In: *Proceedings - International Conference on Image Processing, ICIP* 2017-September, pp. 3645–3649. ISSN: 15224880. DOI: [10.1109/ICIP.2017.8296962](https://doi.org/10.1109/ICIP.2017.8296962). URL: <https://arxiv.org/abs/1703.07402v1>.
- Yoon, Kwangjin et al. (Jan. 2019). "Data Association for Multi-Object Tracking via Deep Neural Networks". In: *Sensors 2019, Vol. 19, Page 559* 19 (3), p. 559. ISSN: 14248220. DOI: [10.3390/S19030559](https://doi.org/10.3390/S19030559). URL: <https://www.mdpi.com/1424-8220/19/3/559>.
- Tsai, Hsieh Fu et al. (Jan. 2019). "Usiigaci: Instance-aware cell tracking in stain-free phase contrast microscopy enabled by machine learning". In: *SoftwareX* 9, pp. 230–237. ISSN: 2352-7110. DOI: [10.1016/J.SOFTX.2019.02.007](https://doi.org/10.1016/J.SOFTX.2019.02.007).
- Anjum, Samreen and Danna Gurari (June 2020). "CTMC: Cell tracking with mitosis detection dataset challenge". In: *IEEE Computer Society Conference on Computer Vision and Pattern Recognition Workshops* 2020-June, pp. 4228–4237. ISSN: 21607516. DOI: [10.1109/CVPRW50498.2020.00499](https://doi.org/10.1109/CVPRW50498.2020.00499).
- Welshhans, Kristy and Gary J. Bassell (July 2011). "Netrin-1-Induced Local β -Actin Synthesis and Growth Cone Guidance Requires Zipcode Binding Protein 1". In: *Journal of Neuroscience* 31 (27), pp. 9800–9813. ISSN: 0270-6474. DOI: [10.1523/JNEUROSCI.0166-11.2011](https://doi.org/10.1523/JNEUROSCI.0166-11.2011). URL: <https://www.jneurosci.org/content/31/27/9800>.
- Sofroniew, Nicholas et al. (Oct. 2021). "napari/napari: 0.4.12rc2". In: DOI: [10.5281/ZENODO.5587893](https://doi.org/10.5281/ZENODO.5587893). URL: <https://zenodo.org/record/5587893>.
- Ioffe, Sergey and Christian Szegedy (Feb. 2015). "Batch Normalization: Accelerating Deep Network Training by Reducing Internal Covariate Shift". In: *32nd International Conference on Machine Learning, ICML 2015* 1, pp. 448–456. URL: <https://arxiv.org/abs/1502.03167v3>.
- Maas, Andrew L, Awni Y Hannun, and Andrew Y Ng (2013). "Rectifier nonlinearities improve neural network acoustic models". In:
- Bodla, Navaneeth et al. (Apr. 2017). "Soft-NMS – Improving Object Detection With One Line of Code". In: *Proceedings of the IEEE International Conference on Computer Vision* 2017-October, pp. 5562–5570. ISSN: 15505499. DOI: [10.1109/ICCV.2017.593](https://doi.org/10.1109/ICCV.2017.593). URL: <https://arxiv.org/abs/1704.04503v2>.
- Kingma, Diederik P. and Jimmy Lei Ba (Dec. 2014). "Adam: A Method for Stochastic Optimization". In: *3rd International Conference on Learning Representations, ICLR 2015 - Conference Track Proceedings*. URL: <https://arxiv.org/abs/1412.6980v9>.

Hart, Peter E., Nils J. Nilsson, and Bertram Raphael (1968). “A Formal Basis for the Heuristic Determination of Minimum Cost Paths”. In: *IEEE Transactions on Systems Science and Cybernetics* 4 (2), pp. 100–107. ISSN: 21682887. DOI: 10.1109/TSSC.1968.300136.